PLANT SCIENCES

Molecular mechanism of trehalose 6-phosphate inhibition of the plant metabolic sensor kinase SnRK1

Jantana Blanford[1]†, Zhiyang Zhai[1]†, Marcel D. Baer[2]†, Gongrui Guo[1], Hui Liu[1], Qun Liu[1], Simone Raugei[2], John Shanklin[1]*

SUCROSE-NON-FERMENTING1-RELATED PROTEIN KINASE1 (SnRK1), a central plant metabolic sensor kinase, phosphorylates its target proteins, triggering a global shift from anabolism to catabolism. Molecular modeling revealed that upon binding of KIN10 to GEMINIVIRUS REP-INTERACTING KINASE1 (GRIK1), KIN10's activation T-loop reorients into GRIK1's active site, enabling its phosphorylation and activation. Trehalose 6-phosphate (T6P) is a proxy for cellular sugar status and a potent inhibitor of SnRK1. T6P binds to KIN10, a SnRK1 catalytic subunit, weakening its affinity for GRIK1. Here, we investigate the molecular details of T6P inhibition of KIN10. Molecular dynamics simulations and in vitro phosphorylation assays identified and validated the T6P binding site on KIN10. Under high-sugar conditions, T6P binds to KIN10, blocking the reorientation of its activation loop and preventing its phosphorylation and activation by GRIK1. Under these conditions, SnRK1 maintains only basal activity levels, minimizing phosphorylation of its target proteins, thereby facilitating a general shift from catabolism to anabolism.

INTRODUCTION

To achieve intracellular homeostasis, all organisms have mechanisms to couple their carbon and/or energy status to decide when to grow and develop and when to conserve energy. In eukaryotes, protein sensor kinases monitor intracellular sugar and energy status and phosphorylate target proteins that regulate the balance between anabolic and catabolic processes. A large, highly conserved protein kinase family, including the yeast sucrose nonfermenting 1 (SNF1), mammalian adenosine monophosphate (AMP)–activated protein kinase (AMPK), and plant SNF1-related protein kinase 1 (SnRK1), plays key roles in this process by fine-tuning intracellular levels of carbon and energy. They typically function as a heterotrimeric complex, consisting of α-catalytic, β- and γ (or β-γ)-regulatory subunits [Polge and Thomas (*1*), Crozet *et al.* (*2*), Crozet *et al.* (*3*)]. The kinase activity of plant SnRK1 is activated when intracellular sugar levels are low, initiating transcriptional activation of transcription factors and/or enzymes involved in catabolism that become inhibited when sugar levels are high, activating energy-demanding anabolic processes [Polge and Thomas (*1*), Figueroa and Lunn (*4*), Zhang *et al.* (*5*), Baena-González *et al.* (*6*)]. The α-catalytic subunit of Arabidopsis SnRK1 is encoded by KIN10 (SnRK1α1/SnRK1.1/AKINα1), KIN11 (SnRK1α2/ SnRK1.2/AKINα2), and KIN12 (SnRK1α3/ SnRK1.2/ AKINα3) [Crozet *et al.* (*3*), Hrabak *et al.* (*7*)]. However, only KIN10 and KIN11 were reportedly expressed in Arabidopsis. While KIN10 is abundantly expressed throughout Arabidopsis tissues, KIN11 expression is more limited [Williams *et al.* (*8*)]. It is well established that the phosphorylated disaccharide trehalose 6-phosphate (T6P) can inhibit SnRK1 activity [Figueroa and Lunn (*4*), Zhang *et al.* (*5*), Zhai *et al.* (*9*), Nunes *et al.* (*10*), Martínez-Barajas *et al.* (*11*)]. Despite its relatively low abundance in plant tissues, T6P is crucial in coordinating and regulating SnRK1 activity [Debast *et al.* (*12*), Eastmond *et al.* (*13*), Fichtner *et al.* (*14*), Gómez *et al.* (*15*)].

Our interest in sensor kinases arose from our discovery that SnRK1 regulates WRINKLED1 (WRI1), the master transcriptional activator of fatty acid synthesis [Zhai *et al.* (*16*)]. Sugar was reported to potentiate the effects of WRI1 expression, because acetyl–coenzyme A, the substrate of fatty acid synthesis, was derived from sugar [Cernac and Benning (*17*)]. However, sugar signaling is also a factor in that under low-sugar conditions, WRI1 is phosphorylated by SnRK1 and subsequently ubiquitinated and degraded by the proteasome [Zhai *et al.* (*16*)]. Increased sugar, or T6P, its intracellular proxy [Fichtner *et al.* (*14*)], inhibits SnRK1, reducing the phosphorylation of WRI1 and its subsequent degradation [Zhai *et al.* (*9*)]. Thus, under high-sugar conditions, WRI1 is not phosphorylated and therefore accumulates, activating the energy-demanding anabolic process of lipid synthesis [Zhai *et al.* (*9*)]. Using microscale thermophoresis (MST), we made precise biophysical measurements of equilibrium dissociation constants to demonstrate that T6P binds to KIN10 at concentrations within its physiological concentration range and that this binding results in KIN10 inhibition. These data were unexpected considering a former view that T6P binds to an intermediary protein that, in complex with T6P, somehow interacts with and regulates SnRK1 [Zhang *et al.* (*5*)]. However, direct binding of T6P to KIN10 is consistent with data from subsequent transgene overexpression studies or mutants that manipulate sugar and/or T6P levels, respectively [Zhai *et al.* (*18*), Zhai *et al.* (*19*)], as previously summarized and reviewed [Zhai *et al.* (*20*)].

Like many protein kinases, SnRK1 has detectable basal activity that is strongly enhanced by the phosphorylation of its α-catalytic subunit KIN10, at a highly conserved threonine ($KIN10^{T175}$, $KIN11^{T176}$) within its activation loop (also known as the T-loop). In Arabidopsis, when T175 was replaced with alanine in catalytic-site mutant $KIN10^{T175A}$, a dominant-negative effect on SnRK1 activity was observed. Conversely, the phosphomimetic mutant $KIN10^{T175D}$ showed constitutively elevated SnRK1 activity compared to native KIN10 [Cho *et al.* (*21*)]. SnRK1-activating kinases SnAK1 and SnAK2, also known as *Arabidopsis Geminivirus Rep* protein-interacting kinases GRIK1 and GRIK2, specifically associate with and phosphorylate the activation loop of SnRK1 [Shen *et al.* (*22*)]. This phosphorylation and SnRK1 activation can be reversed by PP2C phosphatases ABI1 and PP2CA, which can interact

[1]Department of Biology, Brookhaven National Laboratory, Upton, NY 11973, USA. [2]Physical and Computational Sciences Directorate, Pacific Northwest National Laboratory, Richland, WA 99354, USA.
*Corresponding author. Email: shanklin@bnl.gov
†These authors contributed equally to this work.

and dephosphorylate an activated T-loop within KIN10 and KIN11 [Rodrigues *et al.* (*23*)].

While much is known about the biochemistry of SnRK1 control of metabolism, the molecular mechanisms of GRIK1 activation of KIN10 and T6P inhibition of KIN10 remain to be determined. In this work, we used computational chemistry tools to study the molecular mechanism of the T6P inhibition of KIN10, along with a combination of biochemical and biophysical assays to validate our computational studies. Our results show that upon binding to GRIK1, the activation loop of KIN10 undergoes a conformational rearrangement of its T-loop that enables the phosphorylation of T175 required for KIN10 activation. The binding of the negatively charged T6P requires clusters of positive charge on the target protein. Analysis of the KIN10 model identified three non-overlapping positively charged conserved lysine and arginine regions on the surface of KIN10 as candidate T6P binding sites. Computational ligand docking, molecular dynamics (MD) simulations, and in vitro kinase assays identified a highly preferred T6P binding site with a strong T6P binding orientation. Further MD simulations and T6P-KIN10 docking studies identified the mechanism of inhibition of KIN10 whereby upon binding of T6P, its activation loop is prevented from reorienting to the conformation needed to enable its phosphorylation and activation by GRIK1.

RESULTS

Three potential T6P binding sites containing clusters of conserved positively charged residues were identified on the surface of KIN10

To gain insights into the structural details of T6P-KIN10 interactions, we first inspected an alignment of KIN10 homologs from different plant species. We observed conserved positively charged regions containing lysine and arginine residues (fig. S1). Because there is no experimentally determined structure of KIN10, we built a homology model of the KIN10 kinase domain using the crystallographic model of human AMPK catalytic subunit α-2 [Protein Data Bank (PDB) code 5ISO] as a template. We hypothesized that the negatively charged phosphate group on T6P would preferentially bind to clusters of positive charges comprising lysine and arginine residues on the surface of KIN10. We identified three such candidate T6P binding sites, namely, site 1: R23, R32, K34, site 2: R52, R53, K54, and K56, and site 3: K63, R65, and R66 (Fig. 1).

Docking and MD simulations predict stable binding of T6P to site 3

Computational ligand docking studies were performed to identify which of the three sites have the most complementary shape and lowest binding energy. The docking studies identified site 3 as the most promising candidate for T6P binding with poor fits to sites 1 and 2. With site 3, the proposed T6P is located in a shallow hydrophobic pocket, as shown in Fig. 2C. The phosphate group of T6P forms H-bonds with an alkaline patch on KIN10 consisting of K63, R65, R66, and K69, forming a hydrogen bonding network, which may stabilize the phosphate head group. The two sugar rings of T6P form interactions with hydrophobic residues L73, M137, V138, N136, and I166. In addition to ligand docking studies, we performed MD simulations to test the docking results quantitively. Independent simulations initiated with T6P positioned in sites 1 and 2 diffused away from the active residues within 100 ns. In contrast, T6P positioned in site 3 remained bound for the duration of the 400-ns simulation (fig. S2), indicating a (local) free energy minimum, consistent with the docking simulationas most favorable for T6P binding.

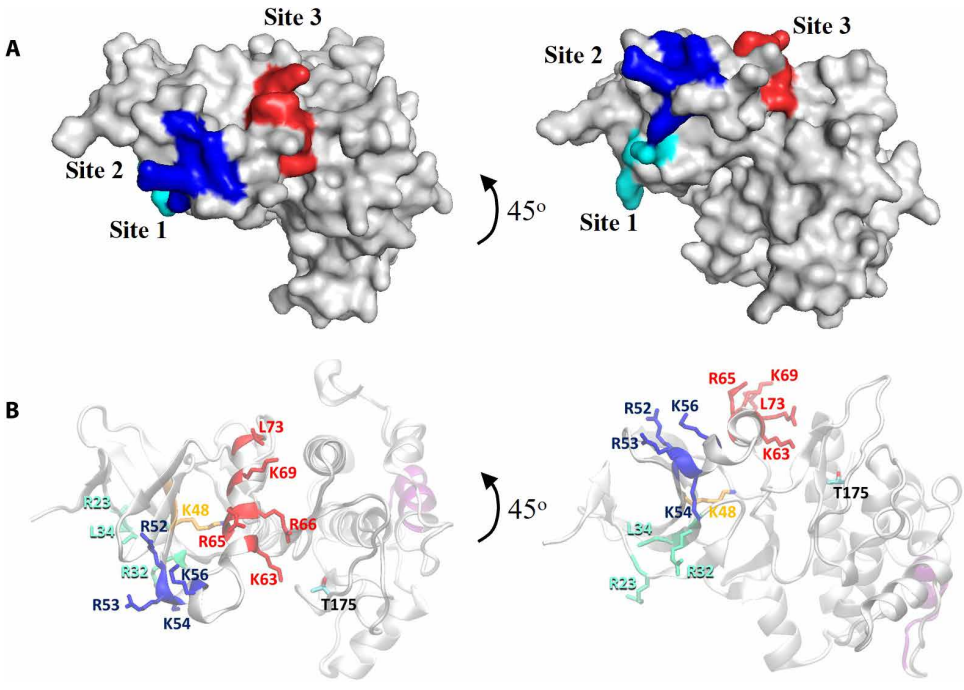

Fig. 1. Arabidopsis KIN10 homology model. (**A**) The space-filling model of the KIN10 homology model shows the locations of predicted T6P binding sites 1, 2, and 3, shown in cyan, blue, and red, respectively. (**B**) The cartoon model of the KIN10 homology model shows amino acid residues in predicted T6P binding site 1 (cyan; R23, R32, and K34), site 2 (blue; R52, R53, K54, and K56) and site 3 (red; K63A-R65A-R66A-K69A-L73A).

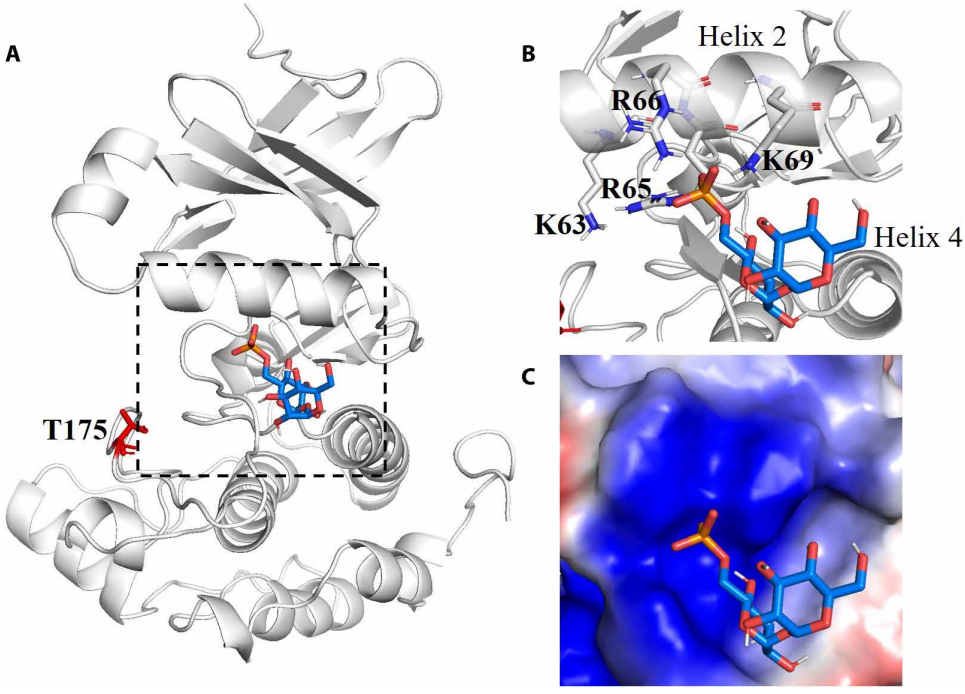

Fig. 2. KIN10-T6P binding model. (**A**) T6P is shown in stick form, and KIN10 is shown as a cartoon. (**B**) Close-up views of T6P binding site 3 on KIN10 (in the dash-lined rectangle). The predicted T6P-interacting residues are shown as stick models. (**C**) Protein electrostatic surface distribution of KIN10. The electrostatic surface was calculated using the protein contact potential program (PyMol). Negatively charged regions are indicated in red, and positively charged regions in blue. (B) and (C) are shown in the same orientation.

Mutation of the three putative T6P binding sites supports only site 3

We tested each of the three candidate T6P binding sites on KIN10 by creating mutants that eliminated their positively charged clusters. The positively charged residues were replaced with neutral alanine residues to create: mutant 1; R23A-R32A-K34A, mutant 2; R52A-R53A-K54A-K56A, and mutant 3; K63A-R65A-R66A-K69A-L73A (Table 1). We then measured equilibrium dissociation constants (K_ds) between KIN10 and T6P using MST. MST analysis showed that T6P bound to wild-type (WT) KIN10 with a K_d of 28 ± 4 μM and showed no significant difference from those of mutants 1 and 2. In contrast, the affinity of T6P binding to mutant 3 was significantly reduced by fivefold at 165 ± 21 μM. The results of these biophysical measurements provide experimental support for the computational predictions of site 3 as the T6P binding site on KIN10. The use of MST for these studies was corroborated by kinase assays that established an inhibitory concentration-50 (IC50) of 40 μM for the inhibition of KIN10 by T6P, which falls well within the expected range for independent validation [Jecklin *et al.* (*24*)].

T6P and adenosine triphosphate binding sites are independent

Protein kinases, including KIN10, use adenosine triphosphate (ATP) as a substrate. Because both ATP and T6P contain phosphate groups, we investigated whether the inhibition of KIN10 by T6P could result from T6P binding to the ATP binding site. To address this question, we performed computational ligand docking. We identified two potential ATP binding modes involving direct interactions with K48, which was previously shown to be a key active site residue [Shen *et al.* (*22*)]. However, both ATP binding modes were spatially separated from the candidate T6P binding sites, as shown in fig. S4. We also further performed MST experiments to determine the K_ds of ATP for both WT KIN10 and mutant 3. Mutant 3, which has a low affinity for T6P, showed no change in the K_d for ATP (fig. S5), which is consistent with the computational docking data presented in fig. S4 that the two binding sites are independent.

KIN10 mutant 3 is insensitive to inhibition by T6P

With computational and biophysical support for site 3 as the T6P binding site on KIN10, we sought to validate the model further using a biochemical assay. We used a well-established KIN10 phosphorylation assay using the sucrose phosphate synthase (SPS) peptide as the substrate [Bhalerao *et al.* (*25*)] to compare the T6P inhibition of KIN10 WT and mutant 3. As described above, KIN10 is activated by GRIK1 and inhibited by T6P. However, KIN10 has basal activity, so we tested WT KIN10 activity in the presence of GRIK1, or GRIK1 plus T6P, and included a control in which only T6P was added to KIN10 (Fig. 3). We expected to see equivalent activity for KIN10 alone and KIN10 plus T6P, but instead, the addition of T6P, the SnRK1 inhibitor, resulted in an approximate doubling of the basal activity of WT KIN10, the SnRK1 α-catalytic subunit. This increase was so unexpected that we repeated the experiment using multiple independent protein preparations, and the differences were highly reproducible and statistically significant. We next tested the activity of mutant 3 in the presence and absence of T6P. In the absence of T6P, mutant 3 basal activity shows a significant increase to approximately twofold that of WT, i.e., equivalent to WT KIN10 in the presence of T6P. Thus, substituting positive charge

Table 1. KIN10 binding affinity to T6P (μM) using MST. MST was performed to determine the equilibrium dissociation constants (K_d) between KIN10 (WT KIN10, KIN10 mutants: 1, 2, and 3) and T6P. Values represent means ± SD over three independent replicates. K_d values for KIN10 mutant 3 and T6P were significantly higher than WT KIN10 ($P < 0.002$ by Student's *t* test of three independent replicates, indicated by an asterisk). The corresponding MST traces are presented in fig. S3.

	Ligand
Target protein	**T6P**
WT	28 ± 4
Mutant 1 (R23A-R32A-K34A)	26 ± 6
Mutant 2 (R52A-R53A-K54A-K56A)	34 ± 5
Mutant 3 (K63A-R65A-R66A-K69A-L73A)	165 ± 21*

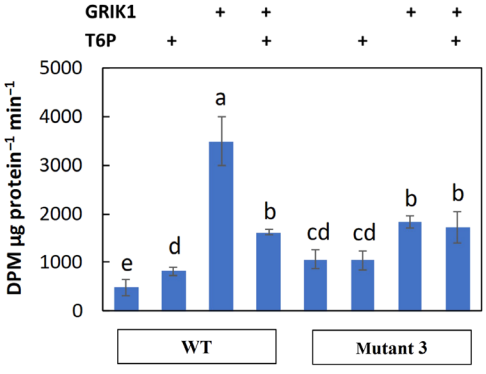

Fig. 3. The KIN10 site 3 mutant shows reduced activation by GRIK1 and insensitivity to T6P inhibition. KIN10 kinase activity was determined by measuring the incorporation of ^{32}P from [γ-^{32}P] ATP into the SnRK1-target peptide, SPS. Kinase activity was quantified for 50 nM KIN10 or a mixture of 50 nM KIN10 plus 50 nM GRIK1 in the absence or presence of 1 mM of T6P. Values represent the mean ± SD of three independent replicates. Levels indicated with different letters above histogram bars are significantly different (Student's *t* test for all pairs, $P < 0.05$). DPM, disintegrations per minute.

in WT by uncharged alanine residues in mutant 3 mimics the binding of T6P. This result is consistent with the reduced activation of only 1.9-fold for mutant 3 in the presence of GRIK1 compared to 4.3-fold for the activation of WT KIN10 by GRIK1. While the WT KIN10 activation is reduced by 66% in the presence of T6P, mutant 3 showed no reduction in its activation, demonstrating its insensitivity to T6P inhibition. In contrast to mutant 3, mutants 1 and 2 whose K_ds for T6P were not significantly different from than that of WT, showed a similar pattern of reduced WT KIN10 activation by GRIK1 in the presence of T6P, which was not observed for mutant 3 (fig. S6).

Identification of potential T6P binding modes within site 3

Having experimentially validated our computationally predicted T6P binding site on KIN10 as site 3, we performed additional computational docking simulations to understand the interactions between T6P and residues lining site 3. Using HADDOCK 2.4 [Dominguez *et al.* (*26*)] and site 3 residues K63, R65, R66, and K69, we identified three candidate binding modes we refer to as A, B, and C (Fig. 4A). Of the three possible binding modes, A comprises 80% of all the structures, while B and C constitute only approximately 10% each. Further refinement of B and C using only residues R65, R66, and K69 led to a 70 and 30% distribution for B and C, respectively. Using active residues K63, R66, R168, and H171 in the refinement for A led to 90% of structures in A and 10% in B (table S1).

The T6P ligand has charged and polar functional groups, suggesting that the most probable stabilizing interactions in the bound state involve charged and polar amino acids. MD simulations were performed to investigate the three binding modes, and the residues in contact with the ligand are highlighted in table S2. In addition, the table includes experimentally mutated residues for comparison. Binding site B shares one residue (R66) in contact with A and one (K69) with C. No residues interacting with T6P are in common between A and C.

Two independent simulations were also carried out as a validation of the docking. The starting positions for each simulation are marked with an X in Fig. 4B. The simulations showed that T6P starting in A stayed within binding mode A throughout the simulation period while the simulation starting in B, sampling of state C, is also observed. Together, these simulations are consistent with the HADDOCK analysis confirming that binding mode A within site 3 primarily contributes to T6P binding.

Experimental and computational results validate KIN10 site 3 mode A as the T6P binding site

To test the influence of several point mutations within mode A of binding site 3, we used MST to measure K_ds of T6P binding to WT, three single mutants (K63A, R66A, and R141A) and a triple mutant (K63A-R66A-R141A). The assays showed that the K_ds of single mutants increased by 1.9- to 2.5-fold that of WT (20.5 ± 3.9 μM). However, the triple mutant showed a sevenfold increase in K_d to 142.8 ± 16.9 μM (Table 2). In addition, MD simulations were performed. During the 200-ns simulations, T6P substrate dissociated almost immediately from the triple mutant but stayed in place throughout the simulation for WT and the three single mutants (Table 2). These results indicate that the loss of negative charges in each of the three key binding residues weakened the interaction between KIN10 and T6P. MST assays and MD simulations prove that K63, R66, and R141 act in concert and are necessary for T6P inhibition of KIN10. The time evolution of contacts between key residues and T6P in the simulations are detailed in figs. S7 to S11.

The flexible KIN10 T-loop contributes to the mechanism of T6P-KIN10 interactions and regulation

While the best homology model, based on the mammalian AMPK 5t5t PDB structure, was used for the binding analysis, other homology models were also compared as the basis for MD simulations. A

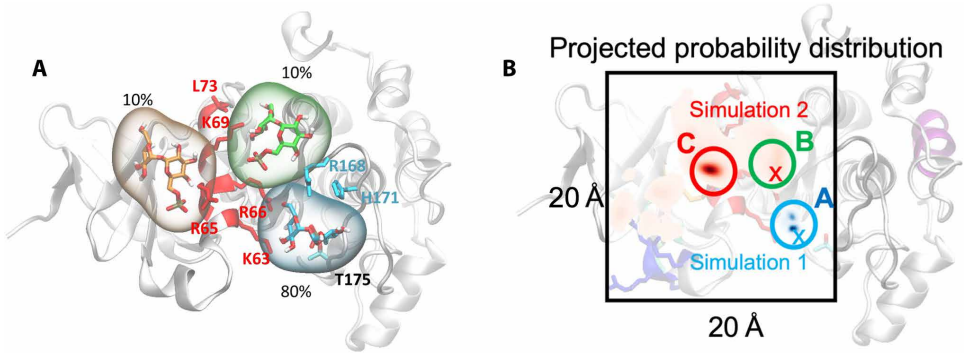

Fig. 4. Three T6P binding modes within binding site 3 were identified, and mode A is the primary binding site for T6P. (**A**) Guided docking using Haddock 2.4 was performed to further refine T6P binding within site 3. Using active residues K63, R65, R66, and K69, the relative populations were given for the three potential local binding modes A (blue), B (green), and C (yellow). (**B**) Projected probability of the position of the T6P obtained from two independent free MD simulations of 400 ns. Starting positions are marked with an X. The simulations sampled three local binding modes labeled A, B, and C, corresponding to the locations in (A). The probability density for simulation started in A and B is shown in blue and red, respectively.

Table 2. The combination of alanine substitutions of T6P-interacting residues significantly weakened the affinity of T6P to KIN10.

	K_ds (μM) determined by MST	MD simulation after 200 ns
Target protein	**Ligand**	
	T6P	
WT KIN10	21 ± 4	Bound
K63A	47 ± 7	Bound
R66A	40 ± 5	Bound
R141A	52 ± 7	Bound
K63A-R66A-R141A	143 ± 17	Unbound

total of 20 homology models were compared, and the results highlighted the importance of the T-loop (i.e., activation loop containing the T175 phosphorylation target residue) as a critical structural feature in the regulation of KIN10. The models are based on crystal structures of the following PDB entries: 5t5t, 6b1u, 4zhx, 6b2e, 4rer, 4qfg, 6c9d, 4rew, 3h4j, 5es1, 4yom, 3fe3, 2qnj, 7jij, 2qnj, 1zmv, 3h4j, 2wzj, 4ynz, and 2hak. The alpha carbons' root means square fluctuation (RMSF) was calculated after aligning all the structures to 5t5t as a reference. The averaged RMSF, highlighting a loop region, shows the most prominent variation among the homology models (Fig. 5, A and B). Upon exploring the free energy of loop conformation (shown in red) for the model based on PDB entry 5t5t using umbrella sampling, the free energy landscape only exhibits a 2-kcal/mol barrier separating the two distinct conformations i.e., loop up, and loop down, which displays equal probability i.e., of 50% for each state (Fig. 5, C and D). Therefore, the flexibility of the loop region could be a critical element in understanding the mechanism of KIN10 regulation by T6P.

The loop region of KIN10 directly interacts with other proteins in the crystal structures for all 20 templates. Four representative examples of different loop conformations and contacts found in the experimental multicomponent homology models (5t5t, 7jhg, 2hak, and 3fe3) are designated as m0, m1, m2, and m3 and presented in fig. S12. HADDOCK scores for T6P docking on these four models indicate that mode A of the m0 model, depicting the loop-up conformation, is the most favorable binding. As expected for an anionic substrate, the largest contribution is electrostatic interaction, which is highest for mode A of the m0 model (table S3). These results suggest that the most energy-favorable binding of T6P is site 3, binding mode A with the T loop-up.

Rearrangement of the KIN10 T-loop during phosphorylation and activation by GRIK1

GRIK1 phosphorylates KIN10 at T175, resulting in its activation [Shen *et al.* (*22*)]. Therefore, the orientation of T175 on the KIN10 activation loop plays a crucial role in its regulation. For example, when the T-loop is in an up conformation, T175 is approximately 23 Å away from K137 in the active site of GRIK1 (Fig. 6, left), while in the loop down conformation, the distance decreases to 8.8 Å (Fig. 6, right). Therefore, the activation loop on KIN10 must reorient by 90° from the up- to the down-conformation to approach the GRIK1 ATP binding site to enable its phosphorylation and activation. Furthermore, docking studies showed that the most stable binding for T6P on KIN10 is mode A in the loop-up conformation, thereby preventing activation by GRIK1.

DISCUSSION

Living organisms are dynamic entities whose intracellular metabolic carbon and energy status constantly change. The availability of carbon

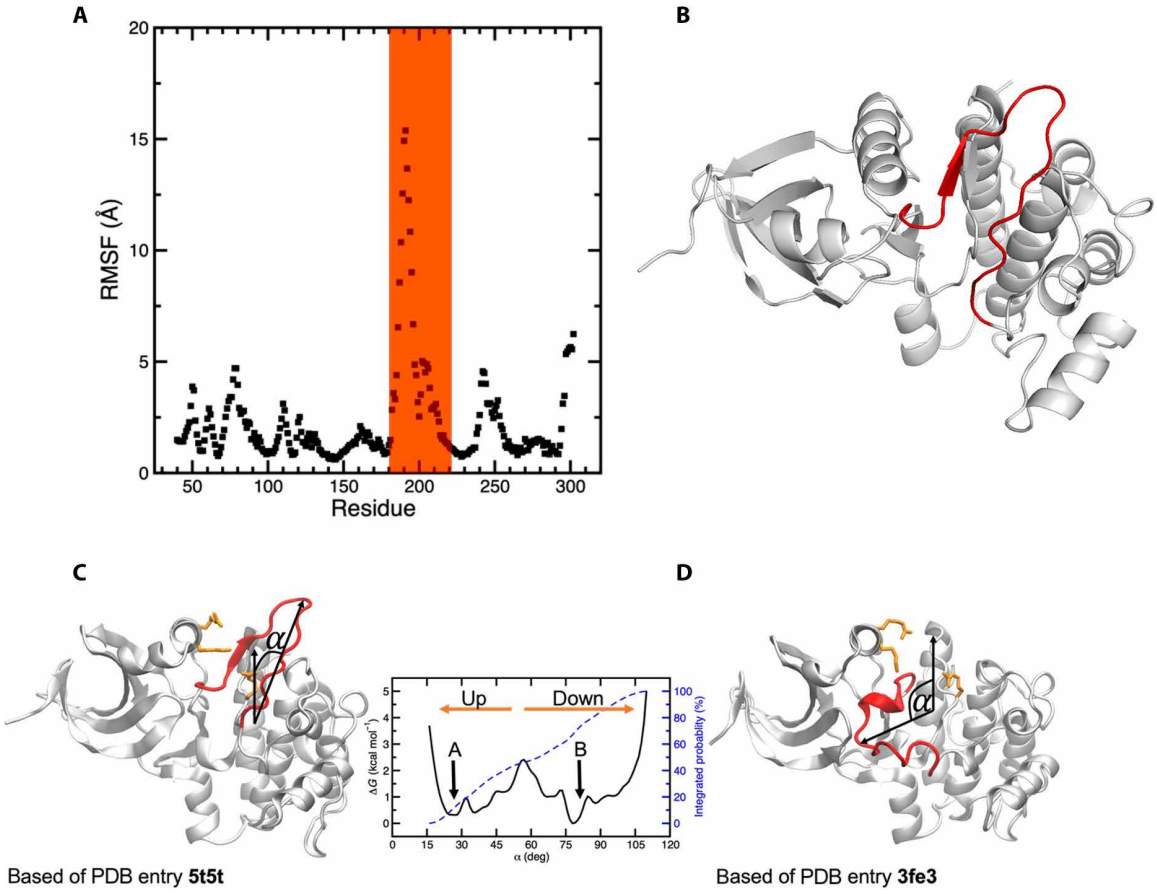

Fig. 5. The largest fluctuations among homology structures occur within the loop region that can exist in two distinct conformations. (**A**) A total of 20 homology models based on PDB entries 5T5T, 6B1U, 4ZHX, 6B2E, 4RER, 4QFG, 6C9D, 4REW, 3H4J, 5ES1, 4YOM, 3FE3, 2QNJ, 7JIJ, 2QNJ, 1ZMV, 3H4J, 2WZJ, 4YNZ, and 2HAK are compared, and the results highlight the importance of the loop region. The RMSF of the α carbons is calculated after aligning all structures to 5T5T as a reference. (**B**) The loop region of the homology structure based on 5T5T is highlighted in red. (**C**) Representative KIN10 homology structures shown with the loop region as the loop up and (**D**) down conformations were modeled on the basis of PDB entries 5t5t and 3fe3, respectively. Simulations were performed by biasing the angle between the center of mass of residues 135 to 157, the center of mass of residues 147 to 157, and residues 188 to 192 in the loop region. The integrated probability of each conformation is shown as the blue dashed line.

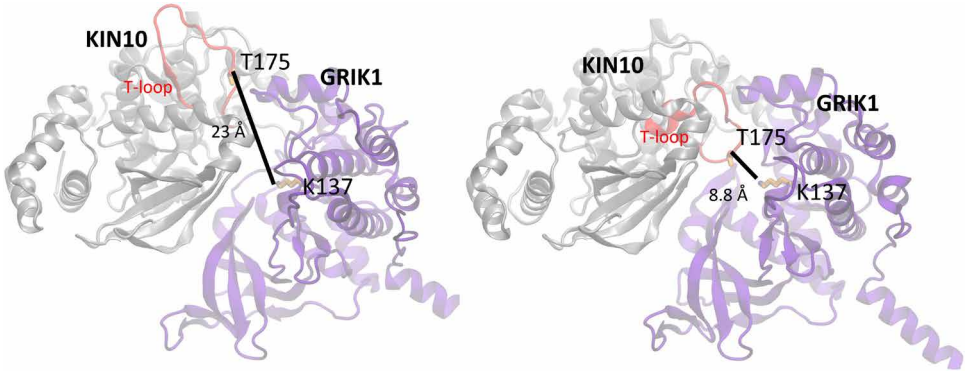

Fig. 6. In the T-loop down orientation, T-175 approaches the GRIK1 active site. The activation loop (red) on KIN10 is near the ATP binding site of GRIK1 during KIN10 phosphorylation by GRIK1. KIN10 is shown in gray, and GRIK1 is shown in magenta.

and energy must be coupled with the regulation of anabolic and catabolic processes and decisions as to carbon allocations to different cellular processes. This coupling is mediated by sensor kinases, including the key SNF1/AMPK/SnRK1 family [Crozet *et al.* (*3*), Broeckx *et al.* (*27*), Crepin and Rolland (*28*)]. The activities of these protein kinases are mediated by their activation or inhibition in response to intracellular signals that act as proxies for cellular carbon and/or energy status. Upon activation, the kinases phosphorylate a constellation of target proteins that mediate the balance between anabolism and catabolism. While the SNF1/AMPK/SnRK1 family shares a common

evolutionary lineage, the cellular signals regulating their phosphorylation activity differ markedly. For example, the mammalian AMPK family is activated by AMP binding to its γ regulatory subunit, a signal of low-energy status. In contrast, the plant α-catalytic subunit of SnRK1 is specifically inhibited by T6P, a phosphorylated disaccharide (and not by other sugar phosphates including sucrose-, glucose-, fructose- or mannose-6 phosphates; table S4.) that acts as a proxy for high carbon, i.e., sugar availability. In either case, the binding of these small molecular regulators results in conformational changes to the kinase that activate or inhibit their activities. While there is a wealth of information regarding the regulatory consequences of sugar status mediated by SnRK1, the molecular details of how T6P binding inhibits the phosphorylation activity of KIN10 have yet to be defined. Until recently, it was generally believed that T6P was bound to an intermediate protein and that this complex interacted with and inhibited the action of SnRK1 [Zhang *et al.* (*5*)]. Using the direct biophysical approach of MST, we established that T6P binds directly to KIN10, the α-subunit kinase of the SnRK1 complex, and that this binding results in a reduction in the affinity of GRIK1 for KIN10 [Zhai *et al.* (*9*)]. However, the reduction of affinity of GRIK1 for KIN10 was only threefold, which was insufficient to explain the reduction in KIN10 activity and prompted us to perform the current studies. We used the KIN10 kinase domain for this work because of its established activity in kinase assays and that it is sensitive to T6P inhibition. Expressing and purifying the full-length KIN10 kinase has yet to be reported. We created a full-length KIN10 protein fused with trigger factor (TF) to investigate whether both the full-length KIN10 and the KIN10 kinase domain respond similarly to T6P inhibition. We compared the inhibition of the TF-full length KIN10 by T6P with that of the KIN10 kinase domain (fig. S13). The data indicates that the TF-full length KIN10 fusion responds similarly to T6P inhibition of kinase activity as the KIN10 kinase domain alone, validating our experimental approach. The main results from the present work extend our previous findings to show the following: (i) T6P binds to KIN10 at a location we refer to as site 3 mode A. (ii) The KIN10 activation T-loop is highly flexible on the basis of comparing the computed root mean square fluctuations and energy calculations. (iii) Modeling of the GRIK1-KIN10 complex shows that the T-loop must be in the down position to enable T175 to approach the GRIK1 active site to enable its phosphorylation and KIN10 activation. (iv) The most stable binding for T6P on KIN10 is site 3, mode A, which causes the T-loop to remain in the up-configuration, thereby preventing its phosphorylation and activation of KIN10 by GRIK1. In Fig. 7 we present a scheme to illustrate the regulation of KIN10 by conformational changes based on the binding of T6P. We use WRINKLED1 as a known substrate of KIN10 that is stabilized in the presence of T6P [Zhai *et al.* (*9*)]. This homeostatic scheme couples levels of the proxy of sugar availability, i.e., T6P, to an energy-demanding anabolic process, namely, fatty acid synthesis, such that it proceeds only when sugar levels are high, and is greatly reduced when energy and sugar levels are insufficient to drive anabolism. Phosphorylation of other KIN10 substrates stimulates catabolism, including starch degradation, and provides a feedback homeostatic mechanism that increases intracellular sugar levels.

SnRK1 and AMPK are controlled by multiple mechanisms that affect kinase activity, stability, and/or subcellular localization [Crozet *et al.* (*3*)]. However, the catalytic α-subunits of both AMPK and SnRK1 polypeptides require phosphorylation at a conserved T-loop threonine for their activation, the allosteric consequences of which differ between the kinases from different kingdoms. For example, AMPK becomes phosphorylated at T172, resulting in its activation. When AMP is bound to the γ-subunit, it stabilizes the interaction between the catalytic and nucleotide modules, preventing the T-loop's dephosphorylation when the AMP to ADP + ATP ratio is low. In the case of AMPK, large-scale domain shifts are stabilized.

In contrast, the mechanism presented herein is that upon binding of GRIK1, the T-loop of KIN10 reorients to present T175 to the GRIK1 active site, promoting its phosphorylation and activation, but the binding of T6P prevents a smaller scale rearrangement of just the T-loop. These mechanisms are fundamentally different in animals where AMP, a low-energy signal, binds to and prevents the

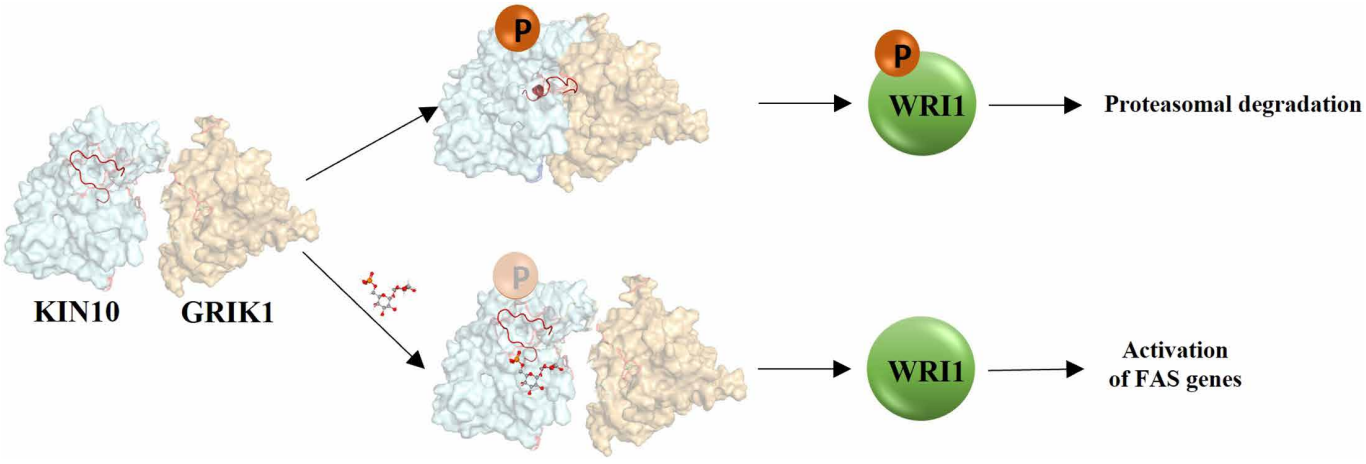

Fig. 7. Proposed molecular details of T6P on the regulation of KIN10 activity with respect to the anabolic process of fatty acid synthesis. The activation loop (red) on KIN10 must approach the GRIK1 ATP binding site to enable the phosphorylation of KIN10 by GRIK1. This phosphorylation enhances KIN10 activity and its phosphorylation of WRI1, committing it to ubiquitin-proteasomal degradation. When the levels of sugar and T6P (shown as a ball-and-stick model) are elevated, it binds to KIN10, reducing its affinity for GRIK1 and preventing its T-loop from achieving the down configuration necessary for its phosphorylation and activation by GRIK1. Activation of KIN10 is thereby reduced, resulting in decreased phosphorylation and degradation of WRI1. Consequently, WRI1 levels increase, activating fatty acid synthesis (FAS) when energy and sugar levels are high.

dephosphorylation of activated AMPK, maintaining its activity. In contrast, in plants, T6P, a signal of high carbon/energy, prevents the reorientation of the KIN10 T-loop necessary for its activation by phosphorylation. While these mechanisms differ within evolutionarily related sensor-kinases, there are some general similarities between the KIN10 mechanism reported herein and that of the two-state paradigm established for distributed feedback grating (DFG)-containing T-loop movements within the human Aurora A kinase using single-molecule fluorescence spectroscopy [Gilburt *et al.* (*29*)]. The Aurora A kinase T-loop exists in dynamic equilibrium between a conserved DFG-in–like active T-loop conformation and a DFG-out–like inactive conformation. In this kinase, the binding of inhibitors freezes the T-loop in the DFG-out–like inactive conformation. However, a critical difference between the Aurora A kinases and KIN10 is that in the DFG-out–like inactive conformation, the Aurora A kinase is inactive but remains phosphorylated. From these and other studies, it is clear that many different mechanisms have evolved to capitalize on the inherent flexibility of kinase T-loops to enable their regulation in diverse cellular contexts across the different kingdoms of life.

MATERIALS AND METHODS

Homology modeling

Arabidopsis KIN10 (Uniprot no. Q38997) kinase domain residues 24 to 364 and GRIK1 (Uniprot no. Q93V58) residues 103 to 396 were used for homolog modeling by using SWISS-MODEL [Biasini *et al.* (*30*)]. The sequence of rat AMPK catalytic subunit alpha-2 (PDB code 5t5t) has a sequence identify of 67.05% with the KIN10 kinase domain, and human Calcium/calmodulin-dependent protein kinase kinase 2 β (PDB code 6bqq) has a sequence identify of 39.3% with GRIK1. Their crystal structures were used as templates for building homology models. Coordinates of residues conserved in targets and template sequences were used directly as a backbone for remodeling insertions and deletions with the build-in procedure implemented in SWISS-MODEL. The KIN10-GRIK1 complex was modeled using AlphaFold [Jumper *et al.* (*31*)]. The five highest-ranked structures are considered to investigate the protein-protein interactions and possible T6P and ATP bindings.

Substrate docking

Potential binding sites of the substrates T6P and ATP were identified using multiple steps. The first step is using the AutoDock Vina [Eberhardt *et al.* (*32*)] as implemented in Chimera [Pettersen *et al.* (*33*)]. Next, the structure for the substrates was generated using Open Babel, and 100 initial structures were generated using the KIN10 kinase domain as a potential binding site, resulting in an initial set of binding sites identified after clustering.

The additional docking simulations for further refinement of binding site 3 were performed using Haddock 2.4 [Dominguez *et al.* (*26*)] server [HADDOCK Web dServer (uu.nl)]. Information about the active protein interface residues was used to drive the docking process within the HADDOCK algorithm. With different starting suggestions for interacting residues, different solutions can be obtained. The identified interacting residues from the initial docking, K63, R65, R66, and K69, were used. For each of the binding sites, 400 structures of the substrate were optimized in explicit water. The resulting complexes were clustered and scored on the basis of the weighted sum of various energy terms (e.g., buried surface area, electrostatic energy, and van der Waals energy).

Protein force field system setup

MD simulations using the all-atom amber03 force field were performed using the Groningen Machine for Chemical Simulations (GROMACS) [Abraham *et al.* (*34*)] MD package. The PDB files for the individual KIN10 and the KIN10-GRIK1 complex, built as described in the homology modeling section, were built using the pdb2gmx tool, assuming pH 7 standard protonation states. Systems were solvated and neutralized with NaCl for charge neutrality using gmx tools. After initial geometry optimization, the systems were run in the NpT ensemble. Simulations were performed with periodic boundary conditions at a temperature of 300 K, maintained by a Nóse-Hoover [Nosé (*35*), Hoover (*36*)] thermostat, and pressure at 1 atm with a Parinello-Rahman [Parrinello and Rahman (*37*), Nosé and Klein (*38*)] barostat. The pressure was maintained. The equations of motion are integrated with the Leap-Frog algorithm with a 2-fs time step and 12-Å cutoff for LJ and Coulombic interactions. The long-range electrostatic was treated under particle mesh Ewald [Essmann *et al.* (*39*)] condition with an interpolation order of 6 and 0.08-nm fast Fourier transform grid spacing.

The parameterization of missing force field parameters for the T6P substrate

Amber03 [Duan *et al.* (*40*)] force field parameters were used to be commensurate with the protein force field. They were generated using the AnteChamber Python Parser interfacE (ACPYPE) [Sousa da Silva and Vranken (*41*)], Python 2.6 [Van Rossum and Drake Jr (*42*)], and Ambertools2019 [Case *et al.* (*43*)] software packages based on a mol2 [Clark *et al.* (*44*)] file generated by openbabel [O'Boyle *et al.* (*45*)] from a SMILES [Weininger (*46*)] (C([C@@H]1[C@H]([C@@H]([C@H]([C@H](O1)O[C@@H]2[C@@H]([C@H]([C@@H]([C@H](O2)COP(=O)(O)O)O)O)O)O)O)O)O) string. The residue was added to the aminoacid.rtp (provided as a plain text file) database within the GROMACS force field directory allows easy system setup from the docked structures using the *pdb2gmx* tool.

MD simulation exploring the identified binding modes within binding site 3

Two independent simulations were started in binding modes A and B within binding site 3 and performed for 400 ns. To analyze the spatial preference of T6P with respect to the protein, a two-dimensional probability distribution is calculated. The protein is rotated as a fixed frame, and the position of the T6P is calculated as the center of mass and projected onto the *xy* plane.

Identification and categorization of residues in contact with T6P

MD simulations were performed for binding modes A, B, and C. A residue is assumed in contact with the T6P if its side chain heavy atoms are within a 5-Å distance from any ligand-heavy atom. Contact residues were categorized into residues tested experimentally by alanine mutation and residues that can be expected to have a critical role based on the charge or polarity of their sidechains.

Umbrella sampling of loop conformation for KIN10 under bulk solvation

The T-loop conformation free energy was explored using umbrella sampling. The initial structures were obtained from a high-temperature NVT simulation starting from loop-up conformation and restraining all but the loop backbone atoms. Each window was simulated without

restraints on the backbone atoms for 60 ns. The collective variable was defined as the angle between the center of mass of residues 135 to 157, the center of mass of residues 147 to 157, and residues 188 to 192 in the loop region.

MD simulations exploring mutations in the binding site

MD simulations were performed to test the influence of several point mutations. The KIN10 and T6P initial configurations were taken from the well-equilibrated simulations. The mutations are introduced into the KIN10 using Chimera, and the system is equilibrated with position restraints on the α carbons and all heavy atoms of the T6P. After the initial equilibration, simulations were performed for 200 ns for each mutation.

KIN10 mutagenesis

The following KIN10 mutants were generated by overlap PCR with KIN10 kinase domain [Zhai *et al.* (*16*)] as DNA template and cloned into pET28a vector between Nde I and Bam HI by In-Fusion with respective pairs of primers listed in table S5: 1(R23A-R32A-K34A), 2 (R52A-R53A-K54A-K56A), 3 (K63A-R65A-R66A-K69A-L73A). Genetic constructs for Native KIN10 and GRIK were described by Zhai *et al.* (*16*).

Expression and purification of recombinant KIN10 mutants and GRIK1

Recombinant KIN10 (including native KIN10 and KIN10 mutants described above) and GRIK1 proteins with N-terminal His6 tags were expressed in *Escherichia coli* BL21(DE3). Protein purification was performed as described by Shen *et al.* (*22*). Briefly, 1 liter of LB medium was inoculated with 10 ml of a saturated growth *E. coli* culture, incubated at 37°C with shaking at 225 rpm until its optical density at 600 nm reached 0.6. At that time, the temperature of the culture was reduced by cooling on ice for 30 min before the addition of isopropyl β-D-1-thiogalactopyranoside to a final concentration of 0.4 mM. The culture was incubated for a further 16 hours at 16°C. Cells were collected by centrifugation at 6000*g* for 15 min at 4°C and resuspended in a lysis buffer containing 20 mM tris-HCl (pH 8.0), 0.5 M NaCl, 10 mM imidazole, and 0.1% (v/v) Triton X-100. The cells were disrupted by triple passage through an EmulsiFlex-C3 (Avestin, Canada; www.avestin.com) at 1000 PSI (6894 kPa). The cell lysate was clarified by centrifugation at 15,000*g* for 30 min at 4°C. The supernatant was applied to a 2-ml Ni-NTA resin column (Qiagen, Hilden, Germany; www.qiagen.com) equilibrated with a lysis buffer supplemented. The column was washed twice with five column volumes of lysis buffer and once with wash buffer [20 mM tris-HCl, pH8.0, 0.5 M NaCl, 30 mM imidazole, and 0.1% (v/v) Triton-X100], and then bound proteins were eluted with 20 mM tris-HCl (pH 8.0), 0.5 M NaCl, 10% (v/v) glycerol supplemented with 500 mM imidazole. The eluted protein samples were desalted using an Econo-Pac 10DG Chromatography Column (Bio-Rad, Hercules, CA; www.bio-rad.com) into 20 mM tris-HCl (pH 8.0), 0.5 M NaCl, 50% glycerol, 1 mM dithiothreitol (DTT). Protein preparations were separated into aliquots and stored at −20°C until use.

Microscale thermophoresis

T6P (purity ≥95%, CAS no.:136632-28-5) was purchased from Santa Cruz Biotechnology. Thermophoretic assays were conducted using a Monolith NT.115 apparatus (NanoTemperTechnologies, South San Francisco, CA; nanotempertech.com). Target proteins (KIN10 and GRIK1) were fluorescently labeled according to the protocol for N-hydroxysuccinimide coupling of the dye NT647 (NanoTemper Technologies) to lysine residues. The target protein and dye were incubated on ice for 30 min. Free dye was separated from labeled protein by size exclusion chromatography using MST buffer [50 mM phosphate buffer (pH 7.4), 150 mM NaCl, 10 $MgCl_2$, 1 mM DTT, and 0.05% (v/v) Tween 20]. For binding tests, 100 nM target protein (fluorescently labeled) was incubated with 50 μM unlabeled ligand for 10 min before the measurement. To determine K_ds, 100 nM target protein was incubated with a serial ligand dilution. Samples of approximately 10 μl were loaded into capillaries and inserted into the MST instrument loading tray (Monolith NT.115). The thermophoresis experiments used 40% MST power and 80% light-emitting diode power at 25°C. T6P (50 μM) was included to test its effect on the associations of KIN10 with ATP or GRIK1.

SnRK1 (KIN10) activity assay

For KIN10 activity assays, purified 50 nM KIN10 or 50 nM KIN10 mutant was included in a 25-μl Kinase Reaction Buffer: 50 mM Hepes-NaOH (pH 7.5), 5 mM $MgCl_2$, 200 μM SPS peptide (RDHM-PRIRSEMQIWSED), 4 mM DTT, 0.5 μM okadaic acid, 0.2 mM ATP, and 12.2 kBq [γ-^{32}P] ATP and incubated at 30°C for 5 min. The assay was stopped by blotting 10 μl per reaction on 4-cm^2 squares of Whatman P81 Phosphocellulose paper (Whatman, Maidstone, UK; Whatman P81 Phosphocellulose paper P81 Ion Exchange Cellulose Chromatography Paper | Lab Alley), immersed in 1% (v/v) phosphoric acid, then washed with four 800-ml volumes of 1% phosphoric acid, immersed in acetone, dried, and transferred to liquid scintillation vials. Liquid scintillation counting using a Tri-carb (PerkinElmer) was used to determine radioactivity associated with phosphorylated SPS peptide [Shen *et al.* (*22*)]. For KIN10 kinase activity assays supplemented with T6P, 1 mM of T6P was added to KIN10 and incubated on ice for 5 min before GRIK1 was added to the reaction.

Accession numbers

Sequence data from this article can be found in The Arabidopsis Information Resource or UniProtKB under the following accession numbers: *KIN10* (At3g01090) and *GRIK1* (At3g45240).

Supplementary Materials

This PDF file includes:

Figs. S1 to S13
Tables S1 to S5

REFERENCES AND NOTES

1. C. Polge, M. Thomas, SNF1/AMPK/SnRK1 kinases, global regulators at the heart of energy control? *Trends Plant Sci.* **12**, 20–28 (2007).
2. P. Crozet, F. Jammes, B. Valot, F. Ambard-Bretteville, S. Nessler, M. Hodges, J. Vidal, M. Thomas, Cross-phosphorylation between Arabidopsis thaliana sucrose nonfermenting 1-related protein kinase 1 (AtSnRK1) and its activating kinase (AtSnAK) determines their catalytic activities. *J. Biol. Chem.* **285**, 12071–12077 (2010).
3. P. Crozet, L. Margalha, A. Confraria, A. Rodrigues, C. Martinho, M. Adamo, C. A. Elias, E. Baena-González, Mechanisms of regulation of SNF1/AMPK/SnRK1 protein kinases. *Front. Plant Sci.* **5**, 190 (2014).
4. C. M. Figueroa, J. E. Lunn, A Tale of Two Sugars: Trehalose 6-Phosphate and Sucrose. *Plant Physiol.* **172**, 7–27 (2016).
5. Y. Zhang, L. F. Primavesi, D. Jhurreea, P. J. Andralojc, R. A. Mitchell, S. J. Powers, H. Schluepmann, T. Delatte, A. Wingler, M. J. Paul, Inhibition of SNF1-related protein kinase1 activity and regulation of metabolic pathways by trehalose-6-phosphate. *Plant Physiol.* **149**, 1860–1871 (2009).

6. E. Baena-González, F. Rolland, J. M. Thevelein, J. Sheen, A central integrator of transcription networks in plant stress and energy signalling. *Nature* **448**, 938–942 (2007).
7. E. M. Hrabak, C. W. Chan, M. Gribskov, J. F. Harper, J. H. Choi, N. Halford, J. Kudla, S. Luan, H. G. Nimmo, M. R. Sussman, M. Thomas, K. Walker-Simmons, J. K. Zhu, A. C. Harmon, The Arabidopsis CDPK-SnRK superfamily of protein kinases. *Plant Physiol.* **132**, 666–680 (2003).
8. S. P. Williams, P. Rangarajan, J. L. Donahue, J. E. Hess, G. E. Gillaspy, Regulation of Sucrose non-Fermenting Related Kinase 1 genes in Arabidopsis thaliana. *Front. Plant Sci.* **5**, 324 (2014).
9. Z. Zhai, J. Keereetaweep, H. Liu, R. Feil, J. E. Lunn, J. Shanklin, Trehalose 6-Phosphate Positively Regulates Fatty Acid Synthesis by Stabilizing WRINKLED1. *Plant Cell* **30**, 2616–2627 (2018).
10. C. Nunes, L. E. O'Hara, L. F. Primavesi, T. L. Delatte, H. Schluepmann, G. W. Somsen, A. B. Silva, P. S. Fevereiro, A. Wingler, M. J. Paul, The trehalose 6-phosphate/SnRK1 signaling pathway primes growth recovery following relief of sink limitation. *Plant Physiol.* **162**, 1720–1732 (2013).
11. E. Martínez-Barajas, T. Delatte, H. Schluepmann, G. J. de Jong, G. W. Somsen, C. Nunes, L. F. Primavesi, P. Coello, R. A. Mitchell, M. J. Paul, Wheat grain development is characterized by remarkable trehalose 6-phosphate accumulation pregrain filling: tissue distribution and relationship to SNF1-related protein kinase1 activity. *Plant Physiol.* **156**, 373–381 (2011).
12. S. Debast, A. Nunes-Nesi, M. R. Hajirezaei, J. Hofmann, U. Sonnewald, A. R. Fernie, F. Börnke, Altering trehalose-6-phosphate content in transgenic potato tubers affects tuber growth and alters responsiveness to hormones during sprouting. *Plant Physiol.* **156**, 1754–1771 (2011).
13. P. J. Eastmond, A. J. van Dijken, M. Spielman, A. Kerr, A. F. Tissier, H. G. Dickinson, J. D. Jones, S. C. Smeekens, I. A. Graham, Trehalose-6-phosphate synthase 1, which catalyses the first step in trehalose synthesis, is essential for Arabidopsis embryo maturation. *Plant J.* **29**, 225–235 (2002).
14. F. Fichtner, J. J. Olas, R. Feil, M. Watanabe, U. Krause, R. Hoefgen, M. Stitt, J. E. Lunn, Functional Features of TREHALOSE-6-PHOSPHATE SYNTHASE1, an Essential Enzyme in Arabidopsis. *Plant Cell* **32**, 1949–1972 (2020).
15. L. D. Gómez, S. Baud, A. Gilday, Y. Li, I. A. Graham, Delayed embryo development in the ARABIDOPSIS TREHALOSE-6-PHOSPHATE SYNTHASE 1 mutant is associated with altered cell wall structure, decreased cell division and starch accumulation. *Plant J.* **46**, 69–84 (2006).
16. Z. Zhai, H. Liu, J. Shanklin, Phosphorylation of WRINKLED1 by KIN10 results in its proteasomal degradation, providing a link between energy homeostasis and Lipid biosynthesis. *Plant Cell* **29**, 871–889 (2017).
17. A. Cernac, C. Benning, WRINKLED1 encodes an AP2/EREB domain protein involved in the control of storage compound biosynthesis in Arabidopsis. *Plant J.* **40**, 575–585 (2004).
18. Z. Zhai, H. Liu, C. Xu, J. Shanklin, Sugar Potentiation of Fatty Acid and Triacylglycerol Accumulation. *Plant Physiol.* **175**, 696–707 (2017).
19. Z. Zhai, J. Keereetaweep, H. Liu, R. Feil, J. E. Lunn, J. Shanklin, Expression of a Bacterial Trehalose-6-phosphate Synthase otsA Increases Oil Accumulation in Plant Seeds and Vegetative Tissues. *Front. Plant Sci.* **12**, 656962 (2021).
20. Z. Zhai, J. Keereetaweep, H. Liu, C. Xu, J. Shanklin, The Role of Sugar Signaling in Regulating Plant Fatty Acid Synthesis. *Front. Plant Sci.* **12**, 643843 (2021).
21. H. Y. Cho, T. N. Wen, Y. T. Wang, M. C. Shih, Quantitative phosphoproteomics of protein kinase SnRK1 regulated protein phosphorylation in Arabidopsis under submergence. *J. Exp. Bot.* **67**, 2745–2760 (2016).
22. W. Shen, M. I. Reyes, L. Hanley-Bowdoin, Arabidopsis protein kinases GRIK1 and GRIK2 specifically activate SnRK1 by phosphorylating its activation loop. *Plant Physiol.* **150**, 996–1005 (2009).
23. A. Rodrigues, M. Adamo, P. Crozet, L. Margalha, A. Confraria, C. Martinho, A. Elias, A. Rabissi, V. Lumbreras, M. González-Guzmán, R. Antoni, P. L. Rodriguez, E. Baena-González, ABI1 and PP2CA phosphatases are negative regulators of Snf1-related protein kinase1 signaling in Arabidopsis. *Plant Cell* **25**, 3871–3884 (2013).
24. M. C. Jecklin, D. Touboul, R. Jain, E. N. Toole, J. Tallarico, P. Drueckes, P. Ramage, R. Zenobi, Affinity classification of kinase inhibitors by mass spectrometric methods and validation using standard IC(50) measurements. *Anal. Chem.* **81**, 408–419 (2009).
25. R. P. Bhalerao, K. Salchert, L. Bakó, L. Okrész, L. Szabados, T. Muranaka, Y. Machida, J. Schell, C. Koncz, Regulatory interaction of PRL1 WD protein with Arabidopsis SNF1-like protein kinases. *Proc. Natl. Acad. Sci. U.S.A.* **96**, 5322–5327 (1999).
26. C. Dominguez, R. Boelens, A. M. Bonvin, HADDOCK: a protein-protein docking approach based on biochemical or biophysical information. *J. Am. Chem. Soc.* **125**, 1731–1737 (2003).
27. T. Broeckx, S. Hulsmans, F. Rolland, The plant energy sensor: evolutionary conservation and divergence of SnRK1 structure, regulation, and function. *J. Exp. Bot.* **67**, 6215–6252 (2016).
28. N. Crepin, F. Rolland, SnRK1 activation, signaling, and networking for energy homeostasis. *Curr. Opin. Plant Biol.* **51**, 29–36 (2019).
29. J. A. H. Gilburt, H. Sarkar, P. Sheldrake, J. Blagg, L. Ying, C. A. Dodson, Dynamic Equilibrium of the Aurora A Kinase Activation Loop Revealed by Single-Molecule Spectroscopy. *Angew. Chem. Int. Ed. Engl.* **56**, 11409–11414 (2017).
30. M. Biasini, S. Bienert, A. Waterhouse, K. Arnold, G. Studer, T. Schmidt, F. Kiefer, T. G. Cassarino, M. Bertoni, L. Bordoli, SWISS-MODEL: modelling protein tertiary and quaternary structure using evolutionary information. *Nucleic Acids Res.* **42**, W252–W258 (2014).
31. J. Jumper, R. Evans, A. Pritzel, T. Green, M. Figurnov, O. Ronneberger, K. Tunyasuvunakool, R. Bates, A. Žídek, A. Potapenko, A. Bridgland, C. Meyer, S. A. A. Kohl, A. J. Ballard, A. Cowie, B. Romera-Paredes, S. Nikolov, R. Jain, J. Adler, T. Back, S. Petersen, D. Reiman, E. Clancy, M. Zielinski, M. Steinegger, M. Pacholska, T. Berghammer, S. Bodenstein, D. Silver, O. Vinyals, A. W. Senior, K. Kavukcuoglu, P. Kohli, D. Hassabis, Highly accurate protein structure prediction with AlphaFold. *Nature* **596**, 583–589 (2021).
32. J. Eberhardt, D. Santos-Martins, A. F. Tillack, S. Forli, AutoDock Vina 1.2.0: New Docking Methods, Expanded Force Field, and Python Bindings. *J. Chem. Inf. Model.* **61**, 3891–3898 (2021).
33. E. F. Pettersen, T. D. Goddard, C. C. Huang, G. S. Couch, D. M. Greenblatt, E. C. Meng, T. E. Ferrin, UCSF Chimera--a visualization system for exploratory research and analysis. *J. Comput. Chem.* **25**, 1605–1612 (2004).
34. M. J. Abraham, T. E. Murtola, R. Schulz, S. Páll, J. C. Smith, B. Hess, E. Lindahl, GROMACS: High performance molecular simulations through multi-level parallelism from laptops to supercomputers. *SoftwareX* **1–2**, 19–25 (2015).
35. S. Nosé, A molecular dynamics method for simulations in the canonical ensemble. *Molec. Phys.* **52**, 255–268 (1984).
36. W. G. Hoover, Canonical dynamics: Equilibrium phase-space distributions. *Phys. Rev. A* **31**, 1695–1697 (1985).
37. M. Parrinello, A. Rahman, Polymorphic transitions in single crystals: A new molecular dynamics method. *J. Appl. Phys.* **52**, 7182–7190 (1981).
38. S. Nosé, M. L. Klein, Constant pressure molecular dynamics for molecular systems. *Molec. Phys.* **50**, 1055–1076 (1983).
39. U. Essmann, L. Perera, M. L. Berkowitz, T. Darden, H. Lee, A smooth particle mesh Ewald method. *J. Chem. Phys.* **103**, 8577–8593 (1995).
40. Y. Duan, C. Wu, S. Chowdhury, M. C. Lee, G. Xiong, W. Zhang, R. Yang, P. Cieplak, R. Luo, T. Lee, J. Caldwell, J. Wang, P. Kollman, A point-charge force field for molecular mechanics simulations of proteins based on condensed-phase quantum mechanical calculations. *J. Comput. Chem.* **24**, 1999–2012 (2003).
41. A. W. Sousa da Silva, W. F. Vranken, ACPYPE - AnteChamber PYthon Parser interfacE. *BMC. Res. Notes* **5**, 367 (2012).
42. G. Van Rossum, F. L. Drake Jr. *Python Reference Manual* (Centrum voor Wiskunde en Informatica Amsterdam, 1995).
43. D. A. Case, I. Y. Ben-Shalom, S. R. Brozell, D. S. Cerutti, T. E. Cheatham, V. W. D. Cruzeiro, T. A. Darden, R. E. Duke, D. Ghoreishi, G. Giambasu, T. Giese, M. K. Gilson, H. Gohlke, A. W. Goetz, D. Greene, R. Harris, N. Homeyer, Y. Huang, S. Izadi, A. Kovalenko, R. Krasny, T. Kurtzman, T. S. Lee, S. LeGrand, P. Li, C. Lin, J. Liu, T. Luchko, R. Luo, V. Man, D. J. Mermelstein, K. M. Merz, Y. Miao, G. Monard, C. Nguyen, H. Nguyen, A. Onufriev, F. Pan, R. Qi, D. R. Roe, A. Roitberg, C. Sagui, S. Schott-Verdugo, J. Shen, C. L. Simmerling, J. Smith, J. Swails, R. C. Walker, J. Wang, H. Wei, L. Wilson, R. M. Wolf, X. Wu, L. Xiao, Y. Xiong, D. M. York, P. A. Kollman, AMBER 2019 (University of California, San Francisco, 2019).
44. M. Clark, R. D. Cramer III, N. Van Opdenbosch, Validation of the general purpose tripos 5.2 force field. *J. Comput. Chem.* **10**, 982–1012 (1989).
45. N. M. O'Boyle, M. Banck, C. A. James, C. Morley, T. Vandermeersch, G. R. Hutchison, Open Babel: An open chemical toolbox. *J. Chem.* **3**, 33 (2011).
46. D. Weininger, SMILES, a chemical language and information system. 1. Introduction to methodology and encoding rules. *J. Chem. Inf. Comput. Sci.* **28**, 31–36 (1988).

Acknowledgments

Funding: This work was supported by the U.S. Department of Energy, Office of Science, Office of Basic Energy Sciences, specifically through the Physical Biosciences program of the Chemical Sciences, Geosciences, and Biosciences Division. J.S. was supported under contract no. DE-SC0012704. Computer time was provided by the National Energy Research Scientific Computing Center (NERSC), a U.S. Department of Energy, Office of Science User Facility operated by Lawrence Berkeley National Laboratory, and the Molecular Sciences Computing Facility (MSCF) in the Environmental Molecular Sciences Laboratory, a DOE User Facility located at the Pacific Northwest National Laboratory (PNNL). Battelle operates PNNL for the DOE under contract number DE-AC05-76RL01830. **Author contributions:** Conceptualization: J.S., J.B., Z.Z., M.D.B., Q.L., and S.R. Formal analysis: J.S., J.B., Z.Z., M.D.B., and S.R. Investigation: J.B., Z.Z., M.D.B., H.L., and G.G. Methodology: J.S., J.B., Z.Z., M.D.B., Q.L., and S.R. Supervision: J.S. and S.R. Writing—original draft: J.B., Z.Z. and M.D.B. Writing—review and editing: J.S., S.R., Q.L., J.B., Z.Z., and M.D.B. **Competing interests:** The authors declare that they have no competing interests. **Data and materials availability:** All data needed to evaluate the conclusions in the paper are present in the paper and/or the Supplementary Materials.

Submitted 28 November 2023
Accepted 15 April 2024
Published 17 May 2024
10.1126/sciadv.adn0895